Using Magnetic Fields to Navigate and Simultaneously Localize Catheters in Endoluminal Environments

Journal Article

Author(s):
Fischer, Cedric; Boehler, Quentin; Nelson, Bradley

Publication date:
2022-07

Permanent link:
https://doi.org/https://doi.org/10.3929/ethz-b-000551965

Originally published in:
IEEE Robotics and Automation Letters 7(3), https://doi.org/10.1109/lra.2022.3181420

Funding acknowledgement:
- Soft Micro Robotics ()
- Arbeitstitel "Soft Magnetic Robots: Modeling, Design and Control of Magnetically Guided Continuum Manipulators" ()
- A Submillimeter Minimally Invasive System for Cardiac Arrhythmia Ablations ()

Using Magnetic Fields to Navigate and Simultaneously Localize Catheters in Endoluminal Environments

Cedric Fischer[1], Quentin Boehler[1] and Bradley J. Nelson[1]

***Abstract*—Remote magnetic navigation offers an ideal platform for automated catheter navigation. Magnetically guided catheters show great dexterity and can reach locations that are otherwise challenging to access. By automating aspects of catheterization procedures, we can simplify and expedite the procedure to allow surgeons to focus on other critical tasks during the surgery. In this article, we describe an automation strategy that is based on the center line of extracted and registered vascular geometries. Position feedback is accomplished with a Hall-effect sensor embedded near the distal end of the catheter. Sensor measurements are compared to the magnetic field predicted by a linear model of the electromagnetic navigation system. By defining specific magnetic field gradients and applying the known vascular geometry, the magnetic fields can be utilized for the simultaneous navigation and localization of the catheter. This eliminates the need for other external, dedicated mapping systems, and the use of fluoroscopy imaging is minimized. The concept is tested in 2d vascular models and the accuracy of the localization is assessed with overhead camera tracking.**

***Index Terms*—Localization; Surgical Robotics: Steerable Catheters/Needles; Surgical Robotics: Planning**

I. INTRODUCTION

REMOTE magnetic navigation (RMN) is an actuation technology that uses magnetic fields to wirelessly manipulate magnetic devices. Minimally invasive surgery is a primary application area of RMN. Medical tools containing magnetic material can be navigated through the human body using external magnetic fields produced by a magnetic navigation system (MNS) [1]. Magnetic actuation allows the catheters to be generally softer and more flexible than their manual counterparts thus reducing the risk of tissue damage during procedures. Forces can be directly applied to the magnetic tip of the catheter offering high dexterity and precision to navigate through complex structures [2], [3]. Hong et al. [4], [5] demonstrated the benefits of a magnetically steered needle for deep brain stimulation by avoiding obstacles along the path. Richter et al. [6] showed that by having two integrated permanent magnets along the catheter, more complex tool shapes can be achieved.

Manuscript received: February 24, 2022; Revised May 6, 2022; Accepted May 23, 2022.

This paper was recommended for publication by Editor Sven Behnke upon evaluation of the Associate Editor and Reviewers' comments. This work was supported by the Swiss National Science Foundation through grant numbers 200020B_185039 and 20B2-1_180861, by the ITC-InnoHK funding, and the ERC Advanced Grant 743217 Soft Micro Robotics (SOMBOT).

[1] Multi-Scale Robotics Lab, ETH Zurich, Switzerland

{fischece,qboehler,bnelson}@ethz.ch

Digital Object Identifier (DOI): see top of this page.

Additionally, RMN offers an ideal platform for automating various surgical procedures. There have been numerous advances in the automation of catheter navigation with remote magnetic navigation [5], [7] and with other traditional methods [8]–[10]. Catheter navigation is a challenging task that is performed by skilled and experienced medical professionals. Automation will enable less experienced clinicians to perform tasks that were previously the domain of highly skilled surgeons and will also simplify and expedite the procedure to allow the practitioners to focus on other critical tasks during the surgery [10].

Tool localization is crucial for automation. However, only a few commercially available mapping methods exist that are compatible with the magnetic fields produced by the MNS. Fluoroscopy is still commonly used for position feedback. But there is an associated health risk to patients and particularly medical staff, thus the aim should be to minimize its usage as much as possible. An alternative is to use a localization method that is based on magnetic field measurements. Hall-effect sensors are inexpensive, accurate, and available in small packages. Several studies have investigated the possibility to localize permanent magnets with Hall sensor arrays placed around the patient [11], [12]. Sharma et al. developed a localization system based on magnetic field gradients [13] in which the Hall-effect sensor is attached to the medical tool that is being localized.

This paper introduces a method for autonomous localization and navigation of catheters in constrained environments that is accomplished with Hall-effect sensor feedback. To automate the catheter steering through a vascular model, the geometry of the structure must be known. The navigation approach described here primarily relies on the center line data of the vascular model and does not rely on a catheter model. The proposed localization method utilizes the known vascular geometry and can locate the integrated Hall-effect sensor inside the catheter by measuring the magnetic field produced by the MNS. This ultimately can make such an MNS a 2-in-1 system as the need for an external, dedicated mapping system can be eliminated as well as the exposure to the ionizing radiation from fluoroscopy imaging can be significantly reduced.

II. MATERIAL & METHODS

A. Electromagnetic Navigation System

We perform the RMN using the CardioMag, an electromagnetic navigation system (eMNS) illustrated in Fig. 1a that

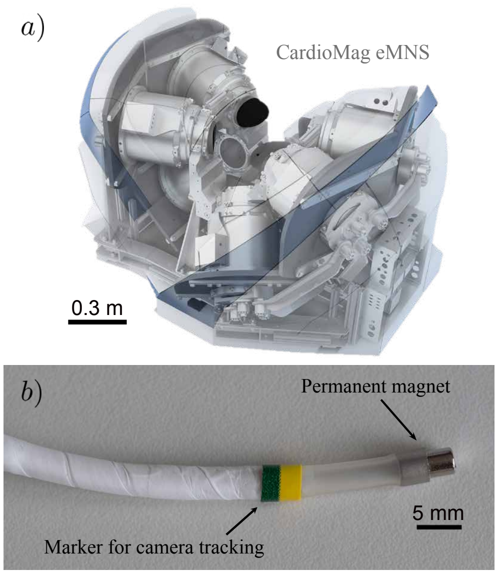

Fig. 1. a) The CardioMag eMNS and b) distal end of the catheter prototype.

consists of eight electromagnets. That allows it to control both the magnetic field $\mathbf{b}(\mathbf{p})$ and the magnetic gradient $\mathbf{g}(\mathbf{p})$ at any position $\mathbf{p} \in \mathbb{R}^3$ within a calibrated volume. A permanent magnet with a dipole moment $\mathbf{m}$ submitted to this field experiences a force $\mathbf{f_m}$ and a torque $\tau_\mathbf{m}$ [14]

$$\mathbf{f_m} = \nabla(\mathbf{m} \cdot \mathbf{b}(\mathbf{p})) \tag{1}$$

$$\tau_\mathbf{m} = \mathbf{m} \times \mathbf{b}(\mathbf{p}). \tag{2}$$

A calibrated field model of the eMNS is used to approximate the individual coils as multiple magnetic dipoles, so that the currents $\mathbf{i} \in \mathbb{R}^8$ in the coils are linearly mapped to the magnetic field and its gradient within a calibrated volume using an actuation matrix $\mathbf{A_m}(\mathbf{p}) \in \mathbb{R}^{8\times 8}$ as [14], [15]

$$\begin{bmatrix} \mathbf{b}(\mathbf{p}) \\ \mathbf{g}(\mathbf{p}) \end{bmatrix} = \mathbf{A_m}(\mathbf{p})\ \mathbf{i} \tag{3}$$

where $\mathbf{g}(\mathbf{p}) = \begin{bmatrix} \frac{\partial b_x}{\partial x} & \frac{\partial b_x}{\partial y} & \frac{\partial b_x}{\partial z} & \frac{\partial b_y}{\partial y} & \frac{\partial b_y}{\partial z} \end{bmatrix}^T$ is the vector composed of the five independent components of the gradient tensor considering $\mathbf{b}(\mathbf{p}) = \begin{bmatrix} b_x & b_y & b_z \end{bmatrix}^T$. A linear field model was used here for sake of convenience, however, the localization method introduced in this study is not limited to a specific field model.

The insertion length of the catheter is controlled by a mechanical catheter advancer (MCA). It is actuated by a Maxon motor and set to a constant insertion speed of 10 mm/s. All inputs to the CardioMag and the MCA are controlled via a Robot Operating System (ROS)-based framework.

B. Magnetic Catheter

The prototype catheter used in this work is depicted in Fig. 1b. It contains a single cylindrical permanent magnet (OD = 3 mm, L = 6 mm) that is attached at the distal end. A PCB mounted Hall sensor (AKM AK09970D with a package size of $1.35\times1.35\times0.57$ mm^3) from Asahi Kasei Microdevices is positioned 12 mm away from the permanent magnet and centered inside the catheter. The sensor has a 16 bit data output with a measurement range of $\pm$ 36 mT on all three axes in its high sensitivity mode. The resulting sensitivity is 1.1 μT/LSB and a sampling frequency of 10 Hz. The sensor measurement is read with an Arduino Uno.

The Hall-effect sensor measures magnetic fields originating from the distal permanent magnet. We assumed this value to be constant during our tests and subtracted it from the sensor measurement beforehand.

The main tubing is made of silicone (Shoreness: 60A, OD = 2.8 mm, ID = 2 mm, Flexan) which is covered in a thin PTFE tape to reduce the friction inside vascular models.The rear section of the catheter contains a PTFE coated stainless steel mandrel (OD = 0.018", McMaster-Carr) to increase the rigidity in order to improve the pushability of the device.

C. Vascular Models

We tested our localization and navigation approach in the vascular models depicted in Fig. 2. The two-dimensional geometries are made from laser-cut POM-C plastic and have a height of 6 mm. The center lines are discretized with an equal spacing of 10 mm along each branch.

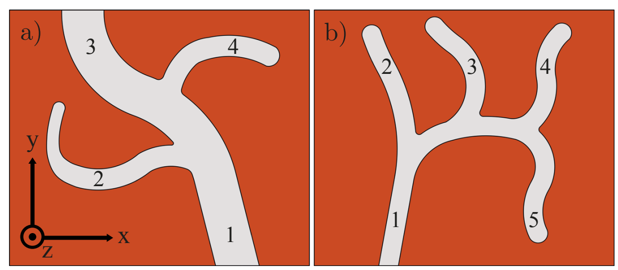

Fig. 2. Vascular models: a) path 1-3 has a width of 24 mm, the side channels are 12 mm wide at their entrances, b) all channels are 11 mm wide.

D. Experimental Setup

The experimental setup is depicted in Fig. 3. The vascular model is mounted on a registered base plate (Thorlabs, Inc.) fixed within the calibrated volume of the CardioMag eMNS. A camera is positioned over the base plate and was used to track the marker on the distal end of the catheter to determine the ground truth position of the Hall sensor during the experiments. The camera view was fed in real-time into ROS and overlaid into a RViz interface of the current localization estimates (see Fig. 3c).

III. Localization

A. Approach

The catheter localization is based on Hall-effect sensor measurements. We measure the magnetic fields from the eMNS and compared these to the calibrated field model to determine the sensor position $\mathbf{p_{est}}$. First, the eMNS calibrated volume within the plane of the models was discretized into a fixed 2d grid. The n grid points were stacked into the point

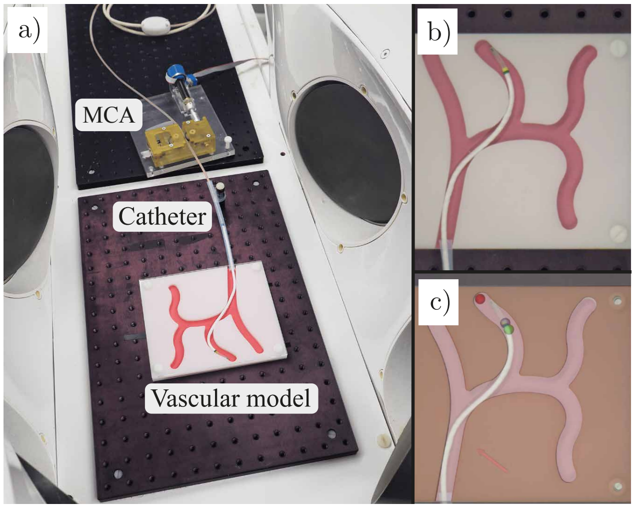

Fig. 3. Experimental setup, a) setup inside CardioMag, b) image view of overhead camera and c) RViz interface in ROS overlaid with camera view: the markers in RViz show the current position estimates (purple and green: for two different gradient settings) and the target position (red).

list $\mathbf{P_{grid}} \in \mathbb{R}^{3\times n}$. The objective of the localization is to find the position in the grid where the error between the measured and predicted magnetic field is minimal. However, a single magnetic field measurement is not enough to find a unique solution to fully determine the actuation matrix $\mathbf{A_m}(\mathbf{p})$ and, ultimately, the sensor position. Furthermore, the sensor orientation is unknown during the navigation procedure. As a consequence, only rotation-invariant parameters can be used, such as the field magnitude, and our optimization task will have multiple solutions.

Autonomous navigation is usually based on pre-operative images from which a geometry of the vascular network can be reconstructed. A 3d mesh of the said geometry can then be registered and overlaid with the actual vasculature by means of, for example, fluoroscopy imaging. Similarly in our case, the position of the geometry must be known with respect to the global frame, as well as the boundaries of the vessels. These geometric constraints can be utilized for the localization process: we know that during the procedure, the catheter is inside the vasculature. This allows us to significantly reduce the search space for the potential sensor positions. Recalling the discretized grid points $\mathbf{P_{grid}}$, all the points of the grid outside the geometry can then be discarded. We denote the remaining point list $\mathbf{P_{ss}} \in \mathbb{R}^{3\times m}$ as the geometric search space to which all magnetic field measurements are compared to (see Fig. 4). To account for potential registration errors during the surgical procedure that could lead to a slight misplacement of the geometry with respect to the eMNS, a looser tolerance on the points to be included in the list $\mathbf{P_{ss}}$ could be considered. The list would increase in size, but the likelihood that all the necessary points for covering the true positions inside the geometry would also increase. To further refine the search space, only the points that are within a predefined distance of 2.5 cm of the previous position estimation are considered for a new position update. We denote this point cloud $\mathbf{P_{ss,local}}$. Any point $\mathbf{p}$ in this point cloud at which the measured magnetic field $\mathbf{b_m}$ meets the condition $|\|\mathbf{b_m}\| - \|\mathbf{b}(\mathbf{p})\|| < \Delta b$ are included in the final matching point cloud $\mathbf{P_{mc}} \in \mathbb{R}^{3\times l}$. The mean value of the remaining points in $\mathbf{P_{mc}}$ is the estimate $\mathbf{p_{est}}$. The restriction of the search space to $\mathbf{P_{ss,local}}$ instead of $\mathbf{P_{ss}}$ also prevents to select candidate points that match in magnitude but are physically not directly connected to the previous position estimate (e.g. matching points that are in another vessel branch). The tolerance Δb set for the magnetic field magnitude depends on multiple factors, such as the grid spacing, the current field magnitude, and the accuracy of the field model and the sensor. This parameter was determined experimentally during testing.

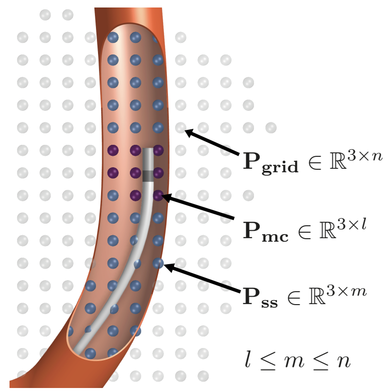

Fig. 4. Visualization of the geometric search space. Discretized grid points in the CardioMag eMNS calibrated volume $\mathbf{P_{grid}}$ (grey), point list $\mathbf{P_{ss}}$ (blue) representing the points of $\mathbf{P_{grid}}$ that are inside the geometry and the point cloud $\mathbf{P_{mc}}$ (purple) which are points of $\mathbf{P_{ss}}$ which match the measured field magnitude $\mathbf{b_m}$.

B. Magnetic gradient control

While the geometric constraints may significantly reduce the amount of points in $\mathbf{P_{mc}}$, there could still be a large positional uncertainty within the geometry. To further reduce the matching point cloud, we set specific magnetic gradients alongside the magnetic fields that are required to navigate the catheters. By applying a magnetic gradient $\mathbf{g}(\mathbf{p_{est}})$ in the direction of the expected largest uncertainty, we generate a larger differentiation across the field magnitudes of points in $\mathbf{P_{ss}}$.

To determine the optimal gradient direction $\hat{\mathbf{u}}_\mathbf{g}$ for an accurate position estimate $\mathbf{p_{est}}$, Principal Component Analysis (PCA) was applied to $\mathbf{P_{ss,local}}$. The dimensionality of the PCA is three for the dimensions of the Cartesian coordinate frame. The output of the PCA is the covariance matrix $\mathbf{C_X}$ [16], which eigenvectors $\mathbf{X_R}$ describe the variability of the points in the vicinity of the current position estimate. The normalized vector $\hat{\mathbf{u}}_\mathbf{g}$ is then obtained as

$$\hat{\mathbf{u}}_\mathbf{g} = \mathbf{X_R} \cdot \frac{\boldsymbol{\lambda_R}}{\sum_{i=1}^{3} \lambda_i} \tag{4}$$

with $\boldsymbol{\lambda_R} = \begin{bmatrix} \lambda_1 & \lambda_2 & \lambda_3 \end{bmatrix}^T$ being the corresponding eigenvalues. The current implementation is limited to a 2d task, with the catheter fully comprised in the xy-plane. In this case, only the orientation of the magnetic field and magnetic field gradient in this plane is required. Considering the following initial, normalized gradient tensor

$$\mathbf{G_{ini}} = \begin{bmatrix} 0.707 & 0 & 0 \\ 0 & -0.707 & 0 \\ 0 & 0 & 0 \end{bmatrix} \quad (5)$$

the optimal gradient tensor $\mathbf{G}$ is obtained by rotating $\mathbf{G_{ini}}$ as

$$\mathbf{G} = \mathbf{R_z}(\theta_{\mathbf{\hat{u}_g}})\,\mathbf{G_{ini}}\,\mathbf{R_z}(\theta_{\mathbf{\hat{u}_f}})^T\, g \quad (6)$$

with

$$\theta_{\mathbf{\hat{u}}} = \mathrm{atan2}(\hat{u}_y, \hat{u}_x) - \frac{\pi}{2} \qquad \text{for} \quad \mathbf{\hat{u}} = \mathbf{\hat{u}_f}, \mathbf{\hat{u}_g} \quad (7)$$

where g is the desired gradient magnitude. The angle $\theta_{\mathbf{\hat{u}}}$ is the angle between the global x-axis and a unit vector $\mathbf{\hat{u}} = \begin{bmatrix}\hat{u}_x & \hat{u}_y & 0\end{bmatrix}^T$, and $\mathbf{R_a}(\theta)$ denotes the rotation matrix of a rotation of angle θ around an axis $\mathbf{a}$. The unit vectors $\mathbf{\hat{u}_f}$ and $\mathbf{\hat{u}_g}$ are the directions of the magnetic field and the magnetic field gradient respectively.

C. Additional magnetic gradient changes

The described primary magnetic gradient setting creates a magnetic field with the highest differentiation along the path direction, thus resulting in the highest localization accuracy along the vessel axis. For the purpose of navigating the catheter through a vessel structure, it is crucial to know the precise insertion length of the catheter within the vasculature in order to change the field accordingly when the catheter approaches a bifurcation. However, at locations where the vessel geometry widens, e.g. at bifurcation or in vessels with a larger diameter, the uncertainty in the radial direction of the vessel may impede the task at hand.

To improve the resolution of the localization, an additional magnetic gradient setting can be applied (see Fig. 5b). By changing the currents to the eMNS once again to generate a larger field differentiation along the main direction of the distribution of the points in cloud $\mathbf{P_{mc}}$, the size of this remaining point cloud reduces which in turn improves the sensor position estimate. This step can be repeated multiple times until there is no further improvement in the localization estimation.

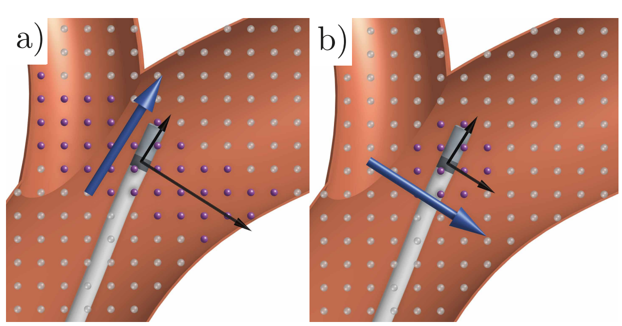

Fig. 5. Matching point cloud $\mathbf{P_{mc}}$ (purple) examples: blue arrows show the magnetic gradient direction, the black arrows the quantitative distribution of $\mathbf{P_{mc}}$, points of $\mathbf{P_{ss}}$ in grey . a) Primary gradient setting gives highest differentiation along vessel axis b) an additional gradient setting can be applied to reduce $\mathbf{P_{mc}}$ and to increase the accuracy of the localization.

IV. Navigation

We aim to automate the catheter navigation through the vascular models shown in Fig. 2 using only the center line information of the geometries. The steps followed for the navigation are detailed in Algorithm 1.

First, the start and end positions are defined. The start position is the current position estimate of the Hall-effect sensor. The target position is selected via an RViz ROS interface. A breadth-first-search path planning algorithm is employed to calculate the path $\mathbf{P_{path}} = [\mathbf{p_1}, \ldots, \mathbf{p_k}] \in R^{3\times k}$ connecting the two positions along the center line points. The path is updated after every iteration of the navigation algorithm. In order to navigate along this path, the magnetic field direction $\mathbf{\hat{u}_f}$ at the current position is defined as follows

$$\mathbf{\hat{u}_f} = \frac{\mathbf{u_f}}{\|\mathbf{u_f}\|} \quad (8)$$

with

$$\mathbf{u_f} = \sum_{i=1}^{h} \mathbf{p_{i+1}} - \mathbf{p_i} \quad (9)$$

which is the sum of the next h tangent vectors along the path. The size h of this horizon depends on the geometry and the discretization step size of the center line and was determined experimentally in this study ($h = 5$). The field magnitude b is kept constant throughout the whole procedure. After every iteration, the MCA is set to insert the catheter by $\Delta L = \mathbf{p_{i+1}} - \mathbf{p_i}$.

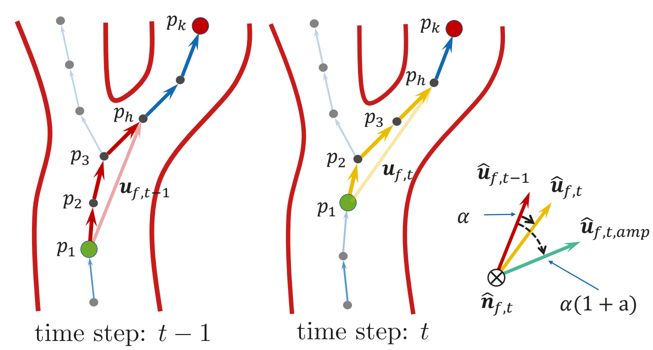

Fig. 6. Visualization of field direction calculation: the example shows two time steps for two consecutive position estimations. On the right, the illustration shows the use of the amplification factor a and the resulting amplified field direction $\mathbf{\hat{u}_{f,t,amp}}$.

The proposed implementation results in field directions that are primarily parallel to the path direction. This strategy involves a certain degree of catheter deflection. The larger the deflection, the higher the increase in the strain potential energy in the catheter caused by its deformation [17]. A constant magnetic torque must be applied to the permanent magnet to keep the catheter in the deflected state. This means that parallel magnetic fields cannot provide enough torque to generate the desired deflections along a path if its direction changes significantly (see (2)).

One way to obtain the necessary magnetic torque is to exaggerate the field changes between two consecutive position estimates along the path. Figure 6 shows an example of this: without further adjustment, the magnetic field is aligned with the calculated directions $\mathbf{\hat{u}_{f,t-1}}$ and $\mathbf{\hat{u}_{f,t}}$ for two consecutive time steps. The field change between these two vectors can be amplified by further rotating $\mathbf{\hat{u}_{f,t}}$ around the normal direction $\mathbf{\hat{n}_{f,t}}$ to obtained the amplified field $\mathbf{\hat{u}_{f,t,amp}}$ as

$$\mathbf{\hat{u}_{f,t,amp}} = \mathbf{R}_{\mathbf{\hat{n}_{f,t}}}(\alpha(1+a))\mathbf{\hat{u}_{f,t-1}} \tag{10}$$

with

$$\mathbf{\hat{n}_{f,t}} = \frac{\mathbf{\hat{u}_{f,t-1}} \times \mathbf{\hat{u}_{f,t}}}{\sin\alpha} \tag{11}$$

where α is the angle between $\mathbf{\hat{u}_{f,t-1}}$ and $\mathbf{\hat{u}_{f,t}}$, and assuming that the path is curved at this position of the trajectory (i.e. $\mathbf{\hat{u}_{f,t-1}}$ and $\mathbf{\hat{u}_{f,t}}$ are not aligned so that $\alpha \neq 0$). The scalar a is a positive amplification factor (see Fig. 6). Examples for no field change amplification ($a = 0$) and a 100% amplification ($a = 1.0$) are depicted in Fig. 7.

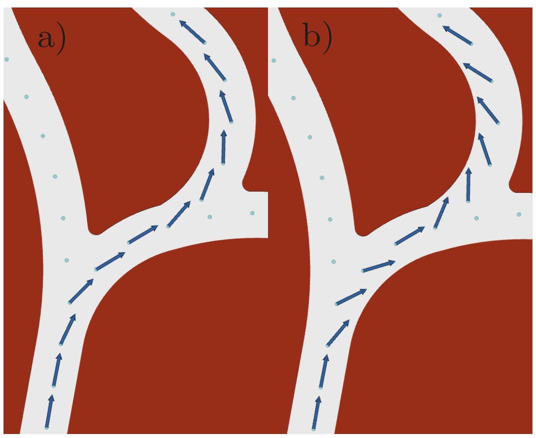

Fig. 7. Field directions $\mathbf{\hat{u}_f}$ along path: a) no field change amplification ($a = 0$), b) field changes amplified by factor $a = 1.0$.

Algorithm 1 Catheter Navigation

Input
$\mathbf{p_i} \leftarrow \mathbf{p_{est}} \in \mathbb{R}^{3\times1}$ ▷ Initial position estimate
$\mathbf{p_n} \leftarrow \mathbf{p_{target}} \in \mathbb{R}^{3\times1}$ ▷ Target position
$\mathbf{P_{cl}} \in \mathbb{R}^{3\times p}$ ▷ List of center line points

Output
$\mathbf{i} \in \mathbb{R}^{8\times1}$ ▷ Current settings for eMNS
ΔL_{MCA} ▷ Adjusted catheter length
$\mathbf{p_{est}} \in \mathbb{R}^{3\times1}$ ▷ Updated position estimate

while target not reached **do**
$\mathbf{P_{path}} \leftarrow PathPlanner(\mathbf{p_{est}}, \mathbf{p_k}, \mathbf{P_{cl}})$
$\mathbf{\hat{u}_f} \leftarrow DetermineFieldDirection(\mathbf{P_{path}})$
$\mathbf{b} \leftarrow \mathbf{\hat{u}_f}\ b$
$\mathbf{\hat{u}_g} \leftarrow PCA(\mathbf{P_{ss,local}})$
$\mathbf{G} = \mathbf{R_z}(\theta_{\mathbf{\hat{u}_g}})\, \mathbf{G_{ini}}\, \mathbf{R_z}(\theta_{\mathbf{\hat{u}_f}})^T g$ ▷ Gradient Tensor
$\mathbf{g} \leftarrow \mathbf{G}$ ▷ extract five indep. components
$\mathbf{b_a} = [\mathbf{b}\, \mathbf{g}] \in \mathbb{R}^{8\times1}$
$\mathbf{A_m} \leftarrow SolveFieldModel(\mathbf{p_{est}})$
$\mathbf{i} \leftarrow \mathbf{A_m}^{-1}\ \mathbf{b_a}$ ▷ Prescribe input currents
$\Delta L_{MCA} \leftarrow \mathbf{p_{path,i+1}} - \mathbf{p_{path,i}}$ ▷ Adjust length
$\mathbf{p_{est}} \leftarrow EstimatePosition(\mathbf{b_m})$ ▷ Update position estimate
if Additional gradient setting is True **then**
$\mathbf{\hat{u}_g} \leftarrow PCA(\mathbf{P_{mc}})$
Repeat same procedure as above
$\mathbf{i} \leftarrow \mathbf{A_m}^{-1}\ \mathbf{b_a}$ ▷ Prescribe input currents
$\mathbf{p_{est}} \leftarrow EstimatePosition()$ ▷ Update estimate
end if
end while

V. Results

A. Hall sensor localization

Table I shows the mean accuracy of the Hall-effect sensor localization method in the vascular models a) and b). In model a), we focused on path 1-3 to investigate the localization accuracy in a wider geometry. In model b), the mean average error of the localization across all paths was 3.64 mm (σ = 1.61 mm) for the primary gradient setting of all estimated positions over a total of 67 measurements. When the direction of the magnetic gradient was changed an additional time, the mean error decreased to 2.74 mm (σ = 1.38 mm).

The tracked path from the main branch 1 to branch 4 can be found in Figure 8. Due to the fact that we use the mean value of $\mathbf{P_{mc}}$ to determine the position estimation, we can see that the initial localization generally has a bias towards the center of the vessels. The mean absolute position error with the primary gradient setting is 3.71 mm. When an additional magnetic gradient change, the accuracy improved to 2.94 mm. However, there was little improvement along the radial axis. The most significant improvement in the localization occurred when navigating past the bifurcation to branch 3: The search space $\mathbf{P_{ss,local}}$ increases and with it, the error of the localization with the primary magnetic gradient setting. We significantly benefited from an additional change to the magnetic gradient in this situation.

This behavior is more pronounced in a wider geometry. Fig. 9 shows the tracked path along the main vessel (1-3) in model a). The additional magnetic gradient setting improved the localization and was able to correctly track the catheter along the right side of the vessel. However, when changing the magnetic gradient, the catheter deflected noticeably several times. This can be seen from the camera tracked path for the primary and subsequent magnetic gradient settings. This deflection decreased the accuracy of the additional gradient setting. The mean error along path 1-3 in model a) was 7.94 mm (σ = 2.94 mm) over 40 measurements for the primary magnetic gradient setting. The additional magnetic gradient improved this number down to 5.65 mm (σ = 2.65 mm) which is less than a quarter of the total width of the vessel.

B. Catheter navigation

The catheter was successfully navigated through all branches of the two geometries by relying solely on the center

TABLE I
LOCALIZATION ERROR DURING NAVIGATION

		Primary gradient setting			Additional gradient setting		
Model	Path	Error (mm)	σ (mm)	Mean err (mm)	Error (mm)	σ (mm)	Mean err (mm)
a	1-3	7.94	2.94	7.94	5.65	2.65	5.65
b	1-2	3.94	0.78	3.64	3.02	1.03	2.74
	1-3	3.45	1.91		1.93	1.47	
	1-4	3.71	1.50		2.94	1.31	
	1-5	3.51	1.91		2.98	1.44	

line information. For these experiments, we used field and gradient magnitudes b and g of 20 mT and 0.15 mT/mm respectively, a tolerance Δb of 0.65 mT, and a workspace grid spacing of 2.5 mm. The tests were conducted with amplification factors a ranging from 0.0 to 1.0. The branches 1 and 3 of the model a), as well as branches 4 and 5 of model b) required some amplification of the field change by at least 0.3 to guarantee successful navigation. There was no significant difference when a was increased further. The test results presented here were achieved with a constant amplification factor of 0.5.

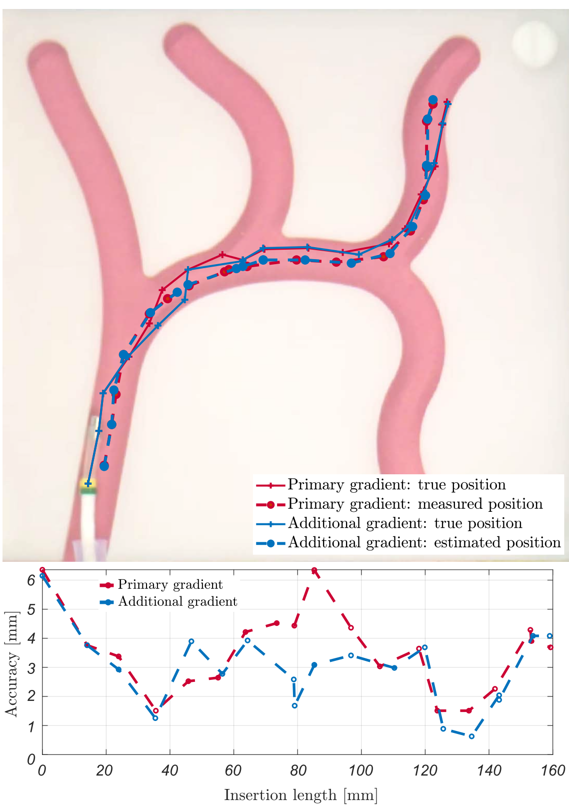

Fig. 8. Comparison of absolute position estimates along a full path in model b) with primary (red) and additional (blue) magnetic gradient settings. The dotted line shows the path tracked by the Hall-effect sensor, the solid line is tracked by the overhead camera.

VI. DISCUSSION & CONCLUSIONS

We have demonstrated a localization method based on Hall-effect measurements with the smallest possible electronics package of one single sensor. With this setup, enough data can be collected to estimate the position of the sensor. The external magnetic fields from the eMNS were used for the navigation and simultaneous localization of a catheter, ultimately making the eMNS a 2-in-1 system: no external, dedicated mapping system is needed during the procedure to acquire the position feedback.

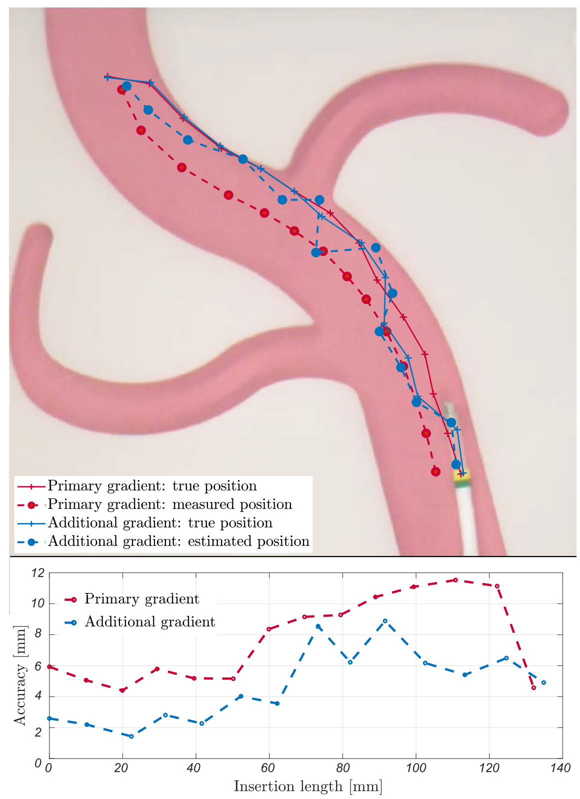

Fig. 9. Comparison of absolute position estimates along a full path in model a) with primary (red) and additional (blue) magnetic gradient settings. The dotted line shows the path tracked by the Hall-effect sensor, the solid line is tracked by the overhead camera.

The localization accuracy was sufficient to navigate the catheter through all branches of the tested vascular models. While axial localization showed promising results in smaller vessels, as expected, the error was higher in the larger vessel or near a bifurcation. In those situations, there are more points in the search space, which in turn increases the possibility to have more points that match the measured field magnitudes. The axial localization generally shows a bias towards the center axis of a vessel structure. However, localization could be improved by changing the direction of the gradient, usually in the radial direction of the vessel. The magnetic gradient could be changed multiple times to improve the estimation even further, albeit with diminishing returns. As we conducted our tests in 2d geometries, we have only tested one additional gradient change. This achieved a 24.73 % improvement on average in the localization accuracy in model b) and 28.83 % in model a). The additional gradient change caused noticeable, unwanted deflections. By keeping the magnetic field constant and only changing the magnetic gradient, the forces exerted on the catheter should remain the same. However, if the field model is solved for a position other than the actual position of the permanent magnet, the magnetic torque acting on the magnet may change and cause a deflection of the catheter. Further improvements in the catheter design, i.e. decreasing the offset between sensor and magnet, could reduce this position mismatch. By lowering the magnitude of the magnetic field during the additional magnetic gradient setting, an unwanted deflection may also be reduced.

To simplify the tests and take advantage of camera tracking to obtain ground truth, we limited our test setups to 2d. In the future, we plan to expand our tests to 3D models. We also plan to test our localization algorithm with other field models such as the one described in Charreyron et al. [1]. The use of a linear model is particularly limited when trying to set specific magnetic gradients which lead the core of the electromagnets to saturate under higher currents [1]. A field model that compensates for the saturation behavior is thus expected to yield better results.

The mean duration time for the position estimation is 38.3 ms (σ = 12.6 ms). It takes 579 ms on average (σ = 29.6 ms) with an i7-6500U (2.5-3.1 GHz) to calculate the new magnetic field and gradient setting. Further optimization of the algorithm could reduce the processing time. The main impediment to the overall procedure time is the slow dynamics of the electromagnets. To improve this, we will limit the actual field changes to situations where it is absolutely necessary, e.g. at bifurcations. The field and gradient settings can be analyzed in advance, optimized for longer sections along the path, and kept constant until the next significant control input is required.

The accuracy of the approach depends on the successful and accurate extraction of the vascular structure and its precise registration during the procedure. As the field directions are directly based on the center line information, the extraction and processing of the center line is crucial, and it currently is a research topic of intense interest [18]–[21].

VII. ACKNOWLEDGMENT

The authors would like to thank Thomas Quirin and Pascal Joris for providing the PCB-mounted Hall sensor.

REFERENCES

[1] S. L. Charreyron, Q. Boehler, B. Kim, C. Weibel, C. Chautems, and B. J. Nelson, "Modeling electromagnetic navigation systems," *IEEE Transactions on Robotics*, vol. 37, no. 4, pp. 1009–1021, 2021.

[2] C. Heunis, J. Sikorski, and S. Misra, "Flexible instruments for endovascular interventions: Improved magnetic steering, actuation, and image-guided surgical instruments," *IEEE Robotics Automation Magazine*, vol. 25, no. 3, pp. 71–82, 2018.

[3] Y. Kim, E. Genevriere, P. Harker, J. Choe, M. Balicki, R. W. Regenhardt, J. E. Vranic, A. A. Dmytriw, A. B. Patel, and X. Zhao, "Telerobotic neurovascular interventions with magnetic manipulation," *Science Robotics*, vol. 7, no. 65, 2022.

[4] A. Hong, Q. Boehler, R. Moser, A. Zemmar, L. Stieglitz, and B. J. Nelson, "3d path planning for flexible needle steering in neurosurgery," *The International Journal of Medical Robotics and Computer Assisted Surgery*, vol. 15, no. 4, p. e1998, 2019.

[5] A. Hong, A. J. Petruska, A. Zemmar, and B. J. Nelson, "Magnetic control of a flexible needle in neurosurgery," *IEEE Transactions on Biomedical Engineering*, vol. 68, no. 2, pp. 616–627, 2021.

[6] M. Richter, V. K. Venkiteswaran, and S. Misra, "Multi-point orientation control of discretely-magnetized continuum manipulators," *IEEE Robotics and Automation Letters*, vol. 6, no. 2, pp. 3607–3614, 2021.

[7] J. Sikorski, C. M. Heunis, F. Franco, and S. Misra, "The armm system: An optimized mobile electromagnetic coil for non-linear actuation of flexible surgical instruments," *IEEE Transactions on Magnetics*, vol. 55, no. 9, pp. 1–9, 2019.

[8] H. A. Jaeger, P. Nardelli, C. O'Shea, J. Tugwell, K. A. Khan, T. Power, M. O'Shea, M. P. Kennedy, and P. Cantillon-Murphy, "Automated catheter navigation with electromagnetic image guidance," *IEEE Transactions on Biomedical Engineering*, vol. 64, pp. 1972–1979, 2017.

[9] A. Schwein, B. Kramer, P. Chinnadurai, N. Virmani, S. Walker, M. O'Malley, A. B. Lumsden, and J. Bismuth, "Electromagnetic tracking of flexible robotic catheters enables "assisted navigation" and brings automation to endovascular navigation in an in vitro study," *Journal of Vascular Surgery*, vol. 67, no. 4, pp. 1274–1281, 2018.

[10] G. Fagogenis, M. Mencattelli, Z. Machaidze, B. Rosa, K. Price, F. Wu, V. Weixler, M. Saeed, J. Mayer, and P. Dupont, "Autonomous robotic intracardiac catheter navigation using haptic vision," *Science Robotics*, vol. 4, no. 29, 2019.

[11] D. Son, S. Yim, and M. Sitti, "A 5-d localization method for a magnetically manipulated untethered robot using a 2-d array of hall-effect sensors," *IEEE/ASME transactions on mechatronics*, vol. 21, no. 2, p. 708–716, 2016.

[12] M.-C. Kim, E.-S. Kim, J.-O. Park, E. Choi, and C.-S. Kim, "Robotic localization based on planar cable robot and hall sensor array applied to magnetic capsule endoscope," *Sensors*, vol. 20, no. 20, 2020.

[13] S. Sharma, A. Telikicherla, G. Ding, F. Aghlmand, A. H. Talkhooncheh, M. G. Shapiro, and A. Emami, "Wireless 3d surgical navigation and tracking system with 100um accuracy using magnetic-field gradient-based localization," *IEEE Transactions on Medical Imaging*, vol. 40, no. 8, pp. 2066–2079, 2021.

[14] J. J. Abbott, E. Diller, and A. J. Petruska, "Magnetic Methods in Robotics," *Annual Review of Control, Robotics, and Autonomous Systems*, vol. 3, no. 1, 2020.

[15] A. J. Petruska, J. Edelmann, and B. J. Nelson, "Model-Based Calibration for Magnetic Manipulation," *IEEE Transactions on Magnetics*, vol. 53, no. 7, 2017.

[16] J. Shlens, "A tutorial on principal component analysis," *CoRR*, vol. abs/1404.1100, 2014.

[17] I. Tunay, "Position control of catheters using magnetic fields," in *Proceedings of the IEEE International Conference on Mechatronics, 2004. ICM '04.*, 2004, pp. 392–397.

[18] F. Oliveira and J. Tavares, "Medical image registration: A review," *Computer methods in biomechanics and biomedical engineering*, vol. 17, pp. 73–93, 01 2014.

[19] H. Sundar, A. Khamene, C. Xu, F. Sauer, and C. Davatzikos, "A novel 2D-3D registration algorithm for aligning fluoro images with 3D pre-op CT/MR images," in *Medical Imaging 2006: Visualization, Image-Guided Procedures, and Display*, vol. 6141.

[20] J. M. Wolterink, R. W. van Hamersvelt, M. A. Viergever, T. Leiner, and I. Išgum, "Coronary artery centerline extraction in cardiac ct angiography using a cnn-based orientation classifier," *Medical Image Analysis*, vol. 51, p. 46–60, Jan 2019.

[21] S. Rjiba, T. Urruty, P. Bourdon, C. Fernandez-Maloigne, R. Delepaule, L.-P. Christiaens, and R. Guillevin, "Centerlinenet: Automatic coronary artery centerline extraction for computed tomographic angiographic images using convolutional neural network architectures," in *IPTA 2020*, 2020, pp. 1–6.